Catalysis Letters (2020) 150:1898–1908
https://doi.org/10.1007/s10562-020-03118-x

Consciously Constructing the Robust NiS/g-C_3N_4 Hybrids for Enhanced Photocatalytic Hydrogen Evolution

Xiao Lin[1] · Shiwen Du[1] · Chunhe Li[1] · Guojun Li[1] · Youji Li[2] · Feitai Chen[2] · Pengfei Fang[1]

Received: 7 November 2019 / Accepted: 21 January 2020 / Published online: 3 February 2020

Abstract

Selective growth of cocatalyst on the surface of photocatalyst has been attracted considerable attention due to their efficient charges transfer property. In this study, the robust NiS modified graphitic carbon nitride (g-C_3N_4) hybrids were successfully synthesized by a facile surface photochemical deposition process. The structure and composition characterization results revealed that the NiS is highly dispersed loading on the surface of g-C_3N_4 nanosheets, and the NiS/g-C_3N_4 hybrids possess large surface areas and excellent optical properties. Under the visible light illumination, the NiS/g-C_3N_4 hybrids with 1.0% weight content of NiS cocatalyst exhibits the highest hydrogen evolution rate of 1346.1 μmol h^{-1} g^{-1} with an apparent quantum efficiency (AQE) of 7.67%. On the basis of photoluminescence (PL) spectra and photoelectrochemical methodology, the photocatalytic hydrogen evolution mechanism was proposed. The results demonstrated that the excellent activity arises from the strong electronic coupling, highly efficient charges separation and migration. This work demonstrates a facile photochemical deposition method to consciously construct the robust two-dimensional (2D) hybrids, so as to realize accurate deposition of cocatalyst and efficient migration of photo-generated carriers.

Graphic Abstract

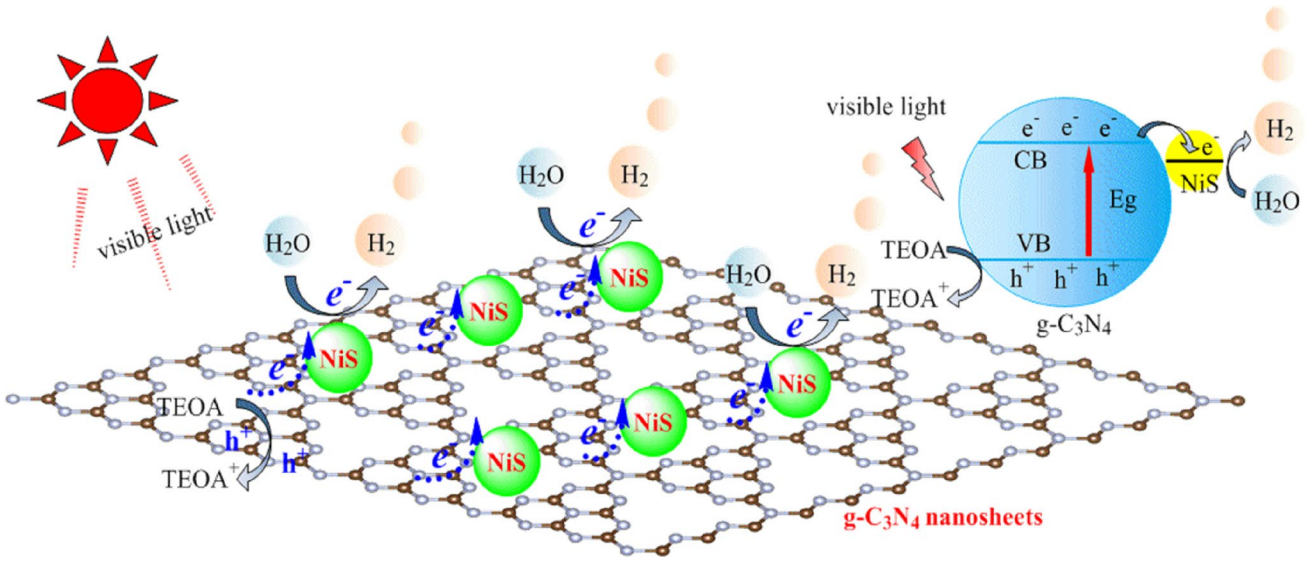

Xiao Lin and Shiwen Du contributed equally to this work.

Electronic supplementary material The online version of this article (https://doi.org/10.1007/s10562-020-03118-x) contains supplementary material, which is available to authorized users.

Extended author information available on the last page of the article

Keywords Photochemical deposition · NiS/g-C_3N_4 · Hydrogen evolution · Thermal oxidation etching

1 Introduction

Environmental pollution and energy crisis are the two major problems for the human to face in the twenty-first century, prompting us to look for renewable and environmentally friendly fuel resources, such as hydrogen energy [1, 2]. It is known that photocatalytic water splitting is one of the most promising strategies to obtain hydrogen energy. To date, numerous researches are focusing on developing efficient, robust, inexpensive, non-pollution and sustainable photocatalytic systems, such as nitrides [3–5], sulfide compounds [6, 7], metal–organic frameworks (MOFs) [8, 9] and oxides based photocatalysts [10, 11]. Among these catalysts, g-C_3N_4 is an emerging and promising photocatalyst for water splitting due to its unique performance. g-C_3N_4 is an expectable n-type semiconductor with a suitable bandgap (2.7 eV) that leads to its light absorption wavelength up to 460 nm, the suitable conduction band (CB) and valence band (VB) position allows it have enough overpotential to realize photocatalytic water splitting [12, 13]. Furthermore, g-C_3N_4 is a non-metallic semiconductor with various advantages such as affordable, non-toxicity, highly thermal and chemical stability. These capabilities made it widely used in many fields, especially photocatalytic hydrogen production from water splitting [14, 15]. However, the application of bulk g-C_3N_4 for photocatalysis is still limited on account of its low surface area, poor utilization of photo-excited charge carriers. This phenomenon may be caused by that the bulk material is consist of 2D layers, which can be easily agglomerated between layers because of the van der Waals force.

Very recently, various measures have been attempted to boost the photocatalytic hydrogen evolution activities of g-C_3N_4, including structure regulations [16], heterojunction creation [17], metal and nonmetal doping [18, 19]. In general, compare to its bulk phase, the ultrathin g-C_3N_4 nanosheets have received much considerable attention on account of its large surface area, exceptional optical and electronic properties. So far, various strategies have been applied to exfoliate bulk g-C_3N_4 into ultrathin 2D nanosheets, including thermal oxidation [20], ultrasonic [21], chemical exfoliation [22] and other methods [23]. These numerous works indicated that the ultrathin g-C_3N_4 nanosheets could be attained successfully and exhibited an excellent performance. However, the intrinsically π-conjugated planes lead to the inefficient and random in-plane charge migration, which resulting in the photo-excited charge carriers hardly migrated to the surface of material for photocatalytic hydrogen generation subsequently [24, 25].

Loading with cocatalyst is another useful method to promoting the migration and separation efficiency of photo-generated carriers, such as Pt, Ag, Au [26–28]. Nevertheless, the rarity and high-cost limited their widespread application. Therefore, it is of great meaningful work to explore earth-abundant and non-noble metal cocatalysts. Recently, transition metal phosphides/sulfides and other complexes function as cocatalysts for enhanced photodriven hydrogen production have garnered considerable attentions [29, 30]. Among these cocatalysts, nickel sulfide (NiS) has received significant attention on account of its low cost, excellent electrical property and highly hydrogen ion trapping capacity. For example, Li et al. successfully synthesized the one-dimensional NiS/CdS nanocomposites by using the solvothermal method, the catalyst showed an enhanced photocatalytic hydrogen evolution performance with a production rate of 1.5 mmol h^{-1} g^{-1} under the visible light illumination [31]. Xin et al. successfully synthesized the ultrathin 2D NiS/TiO_2 nanosheets samples via an in-situ synthesis approach, of which the corresponding hydrogen production rate was 313.6 mmol h^{-1} g^{-1} under the UV–Vis light irradiation [32]. Furthermore, it was reported that the g-C_3N_4 exhibits enhanced hydrogen evolution ability after modified with NiS cocatalyst, which can be prepared by different methods, such as hydrothermal [33], ion-exchange [34] and calcination method [35]. These meaningful efforts are aimed at establishing a good interface contact between the two materials. However, in these photocatalytic systems, NiS was randomly dispersed on the surface of materials. During the photocatalytic hydrogen production process, guides the transmission of photo-generated electrons to the reaction interface is the main function for cocatalyst, and the separation and migration efficiency will be influenced obviously by the loading position [36, 37]. Thus, it is of great significance to design a precise preparation strategy by coupling NiS with photogenic electron outlet on g-C_3N_4.

Inspired but different from the above work, a green and simple template-free photochemical deposition route is used to prepare the NiS/g-C_3N_4 hybrids, anchoring the NiS cocatalyst onto the surface of g-C_3N_4 sheets. The structures, morphologies, chemical compositions, photoelectrical properties and photoactivity of the NiS/g-C_3N_4 hybrids were characterized systematically, the influence of loading amount on hydrogen evolution performance was also discussed. Compared to the bare g-C_3N_4, the NiS/g-C_3N_4 hybrids showed enhanced photocatalytic hydrogen evolution ability. Additionally, the separation and migration mechanism of photon-generated carriers, as well as the synergistic interaction of NiS and g-C_3N_4 were systematically discussed.

2 Experimental Section

2.1 Synthesis of g-C_3N_4 Nanosheets

According to the thermo gravimetric analysis of bulk g-C_3N_4 (Figure S1), g-C_3N_4 nanosheets were prepared by a modified thermal oxidation etching method using urea as the starting material. Briefly, urea was first filled into a crucible with a lid and heated at 550 °C for 3 h with a ramp rate of 5 °C min^{-1}. The ratio of urea to bulk g-C_3N_4 is 5.88%. Then the obtained yellow bulk sample (bulk g-C_3N_4) was grind to powder and heated at 500 °C in air for another 3 h with the same rate.

2.2 Synthesis of NiS/g-C_3N_4 Hybrids

NiS/g-C_3N_4 hybrids were synthesized by a facile photochemical deposition approach, as shown in Figure S2. 0.2 g g-C_3N_4 nanosheets were dispersed in 150 mL ethanol solution (50 vol%) and sonicated for 30 min. Then, 220 μL aqueous solution of $NiCl_2$ (0.1 mol L^{-1}) and 3.5 mg sublimed Sulphur were added, respectively. The suspension was keeping stirring at 70 °C in an water bath for 2 h. After that, the above suspension was irradiated by a 300 W Xe lamp for 3 h under magnetic stirring with the circulating water was 6 °C. The final product was collected by centrifugation and washed with deionized water, anhydrous ethanol and carbon disulfide for several times. After dried in a vacuum oven overnight, the NiS/g-C_3N_4 hybrids photocatalysts were obtained. The NiS/g-C_3N_4 hybrids with different NiS contents (0.1, 0.5, 1.0, 1.5 and 2.0 wt%) were also prepared by changing the amount of $NiCl_2$ and S, which were marked as 0.1% NiS/g-C_3N_4, 0.5% NiS/g-C_3N_4, 1.0% NiS/g-C_3N_4, 1.5% NiS/g-C_3N_4, 2.0% NiS/g-C_3N_4, respectively. For comparison, the NiS modified bulk g-C_3N_4 catalyst (1.0 wt%) was synthesized via the same method as NiS/g-C_3N_4 hybrids except for replacing bulk g-C_3N_4 with g-C_3N_4 sheets, and denoted as 1.0% NiS/g-C_3N_4-bP.

2.3 Material Characterizations and Photocatalytic (Photoelectrochemical) Tests

Full details of the material characterizations, photoelectronchemical tests and photocatalytic hydrogen production are described in the Supplementary Material.

3 Results and Discussion

3.1 Morphology and Microstructure

For purpose of observe the microstructure and morphology of the pure g-C_3N_4 sheets and NiS/g-C_3N_4 hybrids, TEM has been employed. One can see that the pristine g-C_3N_4 sheets show a wrinkled 2D lamellar structure with single or few layers (Fig. 1a, b). This specific structure leads to a large surface area which can serve as a support to bind other particles. The EDS (inset in Fig. 1a) demonstrates the only presence of C and N elements, indicating they are pure g-C_3N_4 sheets. The diffraction peaks of Cu element are appeared in the EDS patterns, which mainly due to the micro grid films are used during the testing process. The TEM images for 2% NiS/g-C_3N_4 hybrids are exhibited in Fig. 1c, d. One can see that the NiS cocatalyst is highly dispersed on the surface of g-C_3N_4 sheets with the diameters about 10 nm. The NiS nanoparticles have unique properties on account of its smaller particle sizes, such as surface effect. This particular structure is beneficial to the formation of the junction/interface between NiS and g-C_3N_4, which could accelerate the separation and migration rate of photo-generated electrons, thus consequently enhancing the hydrogen evolution performance. Compared to the bare g-C_3N_4 sheets, the peaks of C, N, S and Ni elements are observed in the EDS spectrum (inset in Fig. 1c). The elements mapping results of the 2.0% NiS/g-C_3N_4 hybrids are exhibited in Fig. 1e–i. It can be seen that the C, N, S and Ni elements are co-exist and distributed homogeneously in the selected area. The results above demonstrating that the NiS/g-C_3N_4 hybrids were synthesized successfully.

The surface morphologies of obtained catalysts were further observed by SEM, and the results are illustrated in Figure S3. As depictured in Figure S3a, the pure g-C_3N_4 is cotton-like cluster, which assembled by the irregular nanosheets. Figure S3b presents the SEM image of 2.0% NiS/g-C_3N_4 hybrids. It can be seen that there are no obvious changes in the morphologies of g-C_3N_4 after modified with NiS particles. The EDS analysis and elements mapping results of the 2.0% NiS/g-C_3N_4 hybrids are exhibited in Figure S3(c–g). The results are consistent with the TEM elemental mapping, further proved the uniform distribution of NiS particles. Furthermore, the atomic ratio of Ni/S is 1: 1.1, approaching the atomic ratio of NiS, while the atomic ratio of C/N is slightly greater than the atomic ratio of g-C_3N_4 because of the conductive adhesive is used during the testing process. The appeared of Pt signal is resulting from the platinum-spraying during the preparation work for EDS testing. The results discussed above suggest that the NiS/g-C_3N_4 hybrids were synthesized

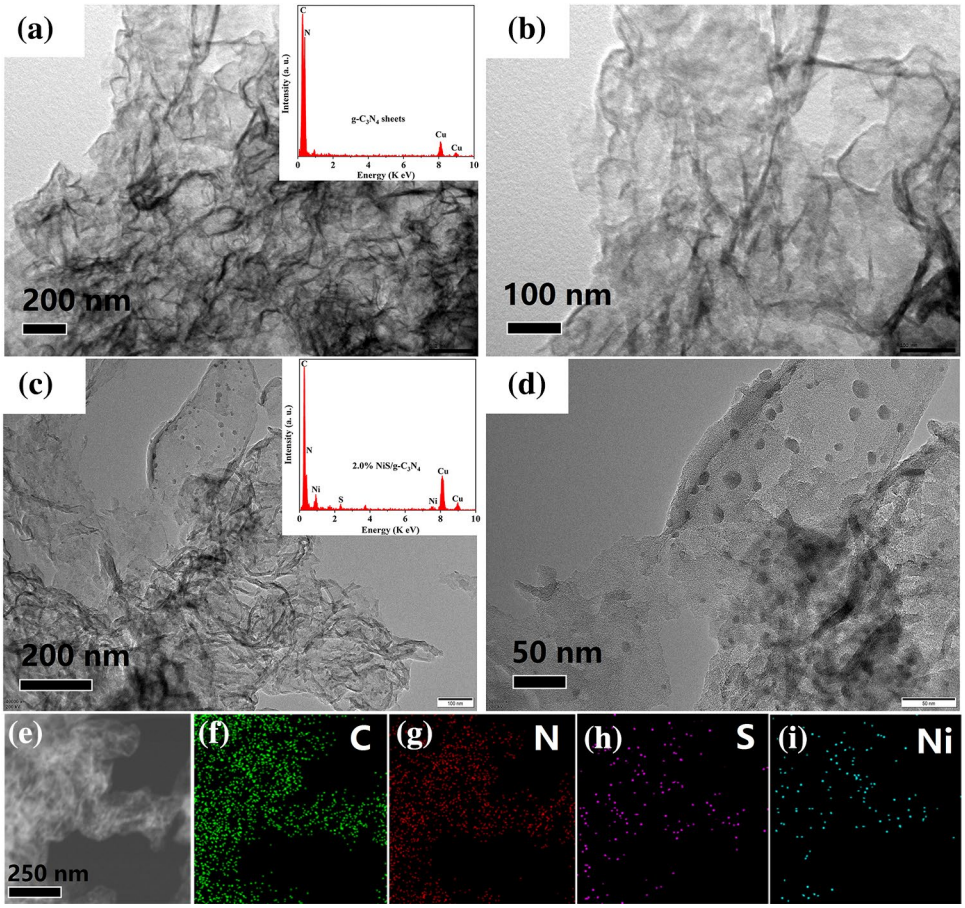

Fig. 1 TEM images of pure g-C_3N_4 sheets (**a**, **b**), 2.0% NiS/g-C_3N_4 hybrids (**c**, **d**) and corresponding elemental mapping images of the C, N, S and Ni elements (**e**–**i**)

successfully, and the NiS cocatalysts are uniformly deposited on the surface of g-C_3N_4 sheets.

3.2 Phase Structure and Surface Chemical State

In order to investigate the changes of phase structure between bulk g-C_3N_4, g-C_3N_4 sheets and NiS/g-C_3N_4 hybrids, the XRD analysis was carry out. According to the Fig. 2a, one can see that the g-C_3N_4 sheets show two uniform diffraction peaks with bulk g-C_3N_4, suggesting that the crystal structures have no obvious changes after thermal oxidation etching. The (100) diffraction peak at $2\theta = 13.1°$ is attributed to the in-plane repeating motifs of the tri-s-triazine units. It is clearly observed that the peak becomes less pronounced, indicating that the planar size is decreased during the thermal oxidation etching process. Meanwhile, the intensity of (002) diffraction peak is also decreased comparison to bulk g-C_3N_4, suggesting a significant weakening of the interlayer stacking. The thinner thickness results in the larger specific surface, which can be further proofed by the BET tests, meaning there are more active sites for the sheets catalysts than bulk g-C_3N_4. Meanwhile, the peak position is shifted from 27.59° to 27.79°, suggesting that the interlayer distance is decreased to 0.321 nm. The heating during thermal oxidation process should lead to a denser packing and thus shorten the gallery distance [20, 38]. So that the photo-generated carriers could easier transport between layers than bulk g-C_3N_4. However, the intensity of diffraction peaks is slightly increased after modified with NiS particles (Fig. 2b), mainly due to the stacking of nanosheets in the drying process. The diffraction peaks of NiS could not be observed in the Fig. 2b, which mainly because of the amorphous feature and the low loading amount of NiS cocatalyst in NiS/g-C_3N_4 hybrids.

Figure 3 gives the XPS spectroscopy of the obtained catalysts, which is used to gain further analyze the composites and surface chemical status. Figure S4 shows the full-spectra survey of pure g-C_3N_4 sheets and NiS/g-C_3N_4 hybrids. Both catalysts show the characteristic peaks of the elements C, N and O. It is should be noted that the O element is detected mainly due to the adsorbed water molecules. The high resolution XPS spectra of C 1s for pure g-C_3N_4 sheets and NiS/g-C_3N_4 hybrids show that there are two peaks located at 284.8, 288.18 eV and 284.8, 288.33 eV, which can be assigned to the correction element or unavoidable adventitious carbon (C–C bonds) and sp^2 carbon in N-containing aromatic nuclei (N–C=N bonds), respectively [39]. Figure 3b shows the typical XPS spectrum for

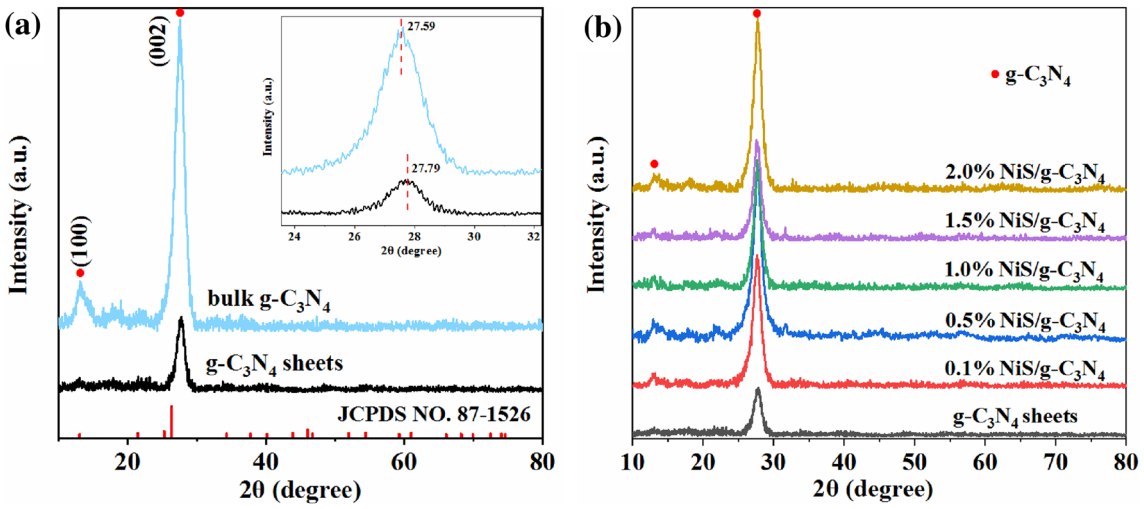

Fig. 2 XRD patterns of bulk g-C_3N_4, g-C_3N_4 sheets and NiS/g-C_3N_4 hybrids with different weight ratios

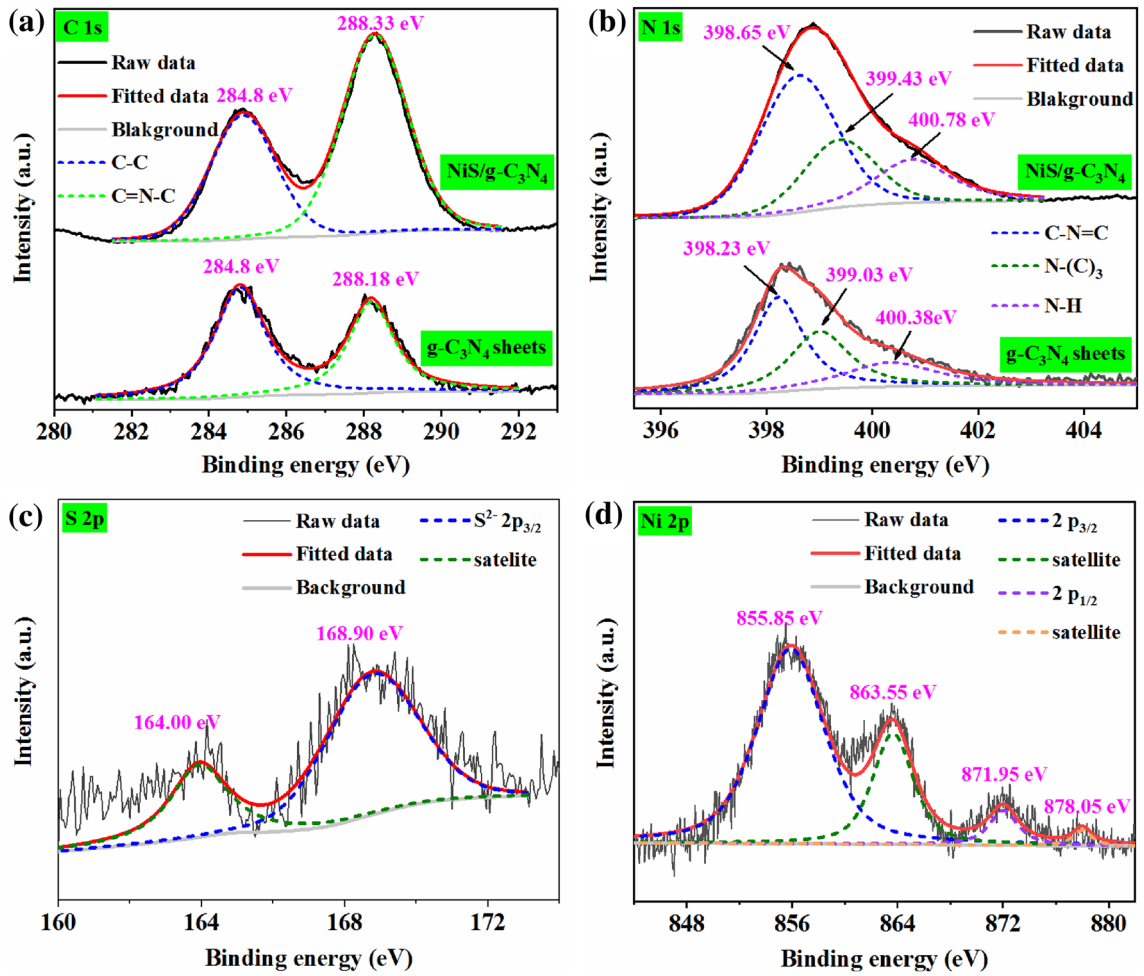

Fig. 3 XPS spectra of **a** C 1s, **b** N 1s, **c** S 2p and **d** Ni 2p of the pure g-C_3N_4 sheets and NiS/g-C_3N_4 hybrids

N 1s in the g-C_3N_4 sheets and NiS/g-C_3N_4 hybrids. The N 1s peaks can be separated to three peaks centered at 398.23, 399.03, 400.38 eV and 398.65, 399.43, 400.78 eV, corresponding to C–N=C groups, tertiary nitrogen N–$(C)_3$ groups and N–H groups, respectively. Meanwhile, compared to the pure g-C_3N_4 sheets, the binding energy of C 1s and N 1s for NiS/g-C_3N_4 hybrids are both positive shifted slightly, evidencing that the electronic density is decreased. This may be caused by the electronic interaction between the elements close-by the interface of NiS/g-C_3N_4 hybrids [40]. Furthermore, the surface-loaded NiS nanoparticles can be demonstrated by the S 2p and Ni 2p XPS spectra (Fig. 3c, d). The peaks observed at 164.00 and 168.90 eV in the S 2p XPS spectrum are attributed to S $2p_{3/2}$ electrons, which can be assigned to the binding energies of S^{2-} ions. The Ni 2p spectrum in Fig. 3d exhibits two peaks located at 855.85 and 871.95 eV can be respectively assigned to the Ni $2p_{3/2}$ electrons and Ni $2p_{1/2}$ electrons, which are related to the characteristic peaks of Ni^{2+} in NiS cocatalyst. The other two peaks located at 863.55 and 878.05 eV are the satellite peaks, consistent with those previous reports [41]. The chemical bonds for different catalysts were further analyzed by FT-IR spectroscopy (Figure S5). Based on the results mentioned above, as well as the XRD and EDS results, one can draw a conclusion that the NiS/g-C_3N_4 hybrids were synthesized successfully. Additionally, the NiS nanoparticles are combined tightly on the surface of g-C_3N_4 nanosheets and forming the schottky heterojunction, so that it will be beneficial for electrons transport during the photocatalytic hydrogen production process.

3.3 Textural and Optical Properties

The Brunauer–Emmett–Teller (BET) method was used to investigate the surface areas and porous structure of g-C_3N_4 and NiS/g-C_3N_4 hybrids. As shown in Figure S6a, the catalysts show a typical type IV adsorption–desorption isotherm based on the IUPAC classification [42]. Moreover, typical H3 hysteresis loops of the obtained catalysts in the high pressure range ($P/P_0 \approx 1.0$) indicate the formation of slit-shaped macropores and mesopores, mainly originate from the aggregating of plate-like g-C_3N_4 nanosheets. In addition, one can see that the bulk g-C_3N_4 also has the characteristic of hysteretic loop of H2 type, showing the blocky shape due to the force between layers. The pore size distributions of the obtained catalysts were tested by the BJH method, and the results show a broadened peak centered at around 2–100 nm, further confirming the presence of mesopores and macropores. The porous structure parameters of bulk g-C_3N_4, g-C_3N_4 sheets and 1.0% NiS/g-C_3N_4 hybrids are obtained and shown in Table S1. Obviously, the surface area of g-C_3N_4 sheets could achieved to 199.23 $m^2\ g^{-1}$, which is approximately 3 times higher than that of bulk g-C_3N_4 (64.25 $m^2\ g^{-1}$), suggesting that the thermal oxidation etching could markedly reduce the thickness of g-C_3N_4. Generally speaking, the reactive contact area and active site are significant influenced by the surface area of catalysts, thus determining the hydrogen production capacity of photocatalyst during the water splitting process. However, the specific surface areas of 1.0% NiS/g-C_3N_4 hybrids decrease to 110.38 $m^2\ g^{-1}$ because of the stacking on nanosheets during the drying process. Interestingly, the pore size increases as the pore diameter decreases after modified with NiS cocatalyst, suggesting that NiS nanoparticles may partially filled in the pores. In summary, the specific structure and the large specific surface area are beneficial to increasing the surface active sites, and thus resulting in improving of the hydrogen production capacity consequently.

In order to gain the light absorption properties of the obtained catalysts, the UV–Vis diffuse reflectance spectroscopy was carried out. It can be observed in Fig. 4a that the g-C_3N_4 nanosheets have an absorption edge at around 447 nm, implying its limited absorption properties under visible light. After modified with NiS nanoparticles, the absorption edges of NiS/g-C_3N_4 hybrids are shift to longer wavelength (red-shift), and the absorbance are also enhanced as the amount of NiS increased. Nonetheless, it doesn't means that the more the better, because the NiS is a black material and cannot be used for photo-driven hydrogen generation directly [31]. The bandgap of obtained catalysts are calculated from the Kubelka–Munk equations. For example, the 1.0% NiS/g-C_3N_4 hybrids have an absorption edge at approximately 464 nm, means a bandgap of 2.67 eV, which is observably narrower than that of pristine g-C_3N_4 sheets (2.78 eV). The changes in bandgap can be attributed to the tight interfacial junction between NiS and g-C_3N_4 nanosheets. The narrower bandgap means the wider responses range of visible light, thus, the improved generation efficiency of the photon-generated carriers can be obtained. In a word, the slightly bandgap narrowing and the improved visible light harvesting ability of NiS/g-C_3N_4 hybrids might be beneficial to enhancing its hydrogen production activity.

To further investigate the migration and recombination behavior of the photo-generated carries during the photocatalytic hydrogen evolution process, the steady-state PL measurement was employed. Figure 4b presents the PL spectra of pristine g-C_3N_4 sheets and NiS/g-C_3N_4 hybrids. A strong and wide PL excitation peak can be observed at approximately 438 nm for bare g-C_3N_4 catalyst, means that a higher recombination rate occurred on photo-generated electrons and holes in the g-C_3N_4 sheets. The PL intensity is clearly decreased after loaded with NiS cocatalyst, suggesting a lower recombination rate between the photo-generated electrons and holes in NiS/g-C_3N_4 hybrids. This phenomenon can be explained by the formation of Schottky

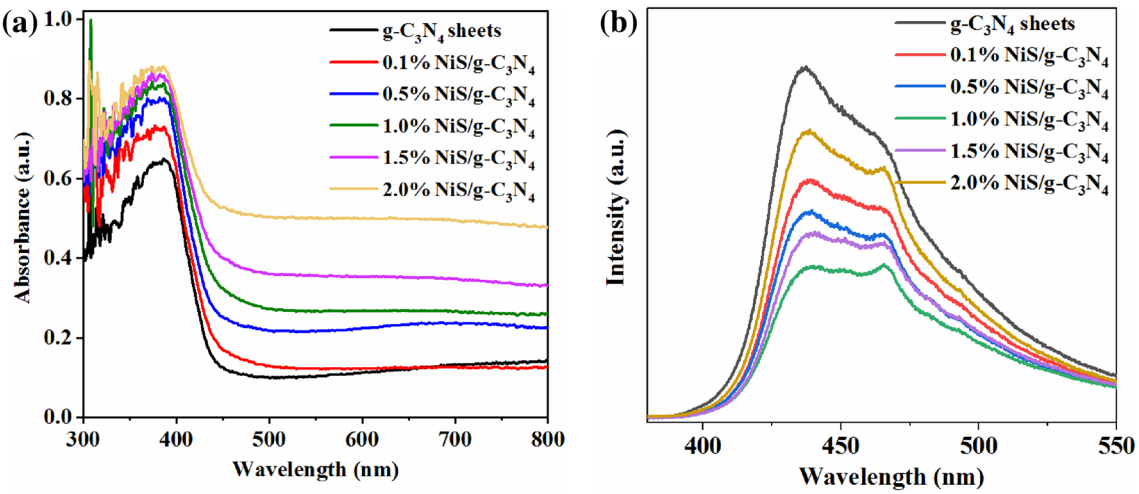

Fig. 4 UV–Vis diffuse reflectance spectra (**a**), PL spectra (**b**) of pure g-C_3N_4 sheets and NiS/g-C_3N_4 hybrids

heterojunction between NiS and g-C_3N_4 sheets, thus, the rapid separation and migration rate of photo-generated electrons and holes is realized.

3.4 Photoelectrochemical Test

To further study the separation and transfer behavior of photo-generated charge carriers of bare g-C_3N_4 and NiS/g-C_3N_4 hybrids, the photoelectrochemical analysis was employed subsequently. Figure 5a gives the transient photocurrent-time (I-t) curves of the bare g-C_3N_4 sheets and NiS/g-C_3N_4 hybrids. It can be seen that all the samples show relatively stable periodic switching photocurrent response under the visible light irradiation. When the light turned on, the photocurrents immediately increase to a stable level, and rapidly decrease to zero when light turned off. The NiS/g-C_3N_4 hybrids with different loading weight all show enhanced photocurrent than pure g-C_3N_4 sheets, and the maximum value of the photocurrent can be reached when the loading weight of NiS cocatalyst is set to 1.0 wt%. As is well-known, the photocurrent is generated mainly due to the separation of photocatalytic e^-/h^+ pairs at the interface of electrode and electrolyte [17]. Accordingly, these results indicate that modifying with NiS nanoparticles could enhance the separation efficiency of photo-generated e^-/h^+ pairs, thus improving the hydrogen production ability. Figure 5b exhibits the LSV polarization curves for bare g-C_3N_4 and NiS/g-C_3N_4 hybrids with a sweep rate of 10 mV/s. The NiS/g-C_3N_4 hybrids show a quite higher electrocatalytic activity than pristine g-C_3N_4 sheets, and the 1.0% NiS/g-C_3N_4 hybrids can achieve the optimal value. These results indicate that the NiS cocatalyst loading could effectively reduce the overpotential and accelerate the electrocatalytic hydrogen evolution kinetics of the NiS/g-C_3N_4 hybrids. Moreover, the surface charge transfer resistance of different samples was investigated by the electrochemical impedance spectroscopy (EIS) analysis. Generally speaking, the transfer resistance of electrons is related to the diameter of semicircular portion from the Nyquist diagrams, and the smaller radius means the lower resistance, suggesting the higher separation and transfer efficiency of photo-generated carriers [43]. According to Fig. 5c, the NiS/g-C_3N_4 hybrids have a faster interfacial electrons transfer than pristine g-C_3N_4 sheets, and the 1.0% NiS/g-C_3N_4 hybrids have the highest separation and migration efficiency in photon-generated e^-/h^+ pairs. Figure 5d exhibits the Bode plots of pristine g-C_3N_4 sheets and NiS/g-C_3N_4 hybrids. All the NiS/g-C_3N_4 hybrids show lower |Z| value than pristine g-C_3N_4 sheets. The 1.0% NiS/g-C_3N_4 hybrids have the minimum value, meaning the fastest electron transfer rates among all catalysts can be obtained. These results demonstrate that after modified with NiS cocatalyst, the separation efficiency and transfer rates of photon-generated carriers are improved remarkably, thus enhancing the photocatalytic hydrogen evolution performance of the catalyst.

3.5 Photocatalytic Hydrogen Evolution Performance

The photocatalytic hydrogen evolution performance of the obtained catalysts was evaluated under the visible light irradiation ($\lambda \geq 400$ nm) using TEOA as the sacrificial reagent. Figure 6a shows the time dependent amount of hydrogen yield over pristine g-C_3N_4 sheets and NiS/g-C_3N_4 hybrids. One can see that the hydrogen production of pristine g-C_3N_4 sheets is almost negligible under the visible light, which mainly on account of the fast recombination between photo-generated e^-/h^+ pairs. Miraculously, the hydrogen

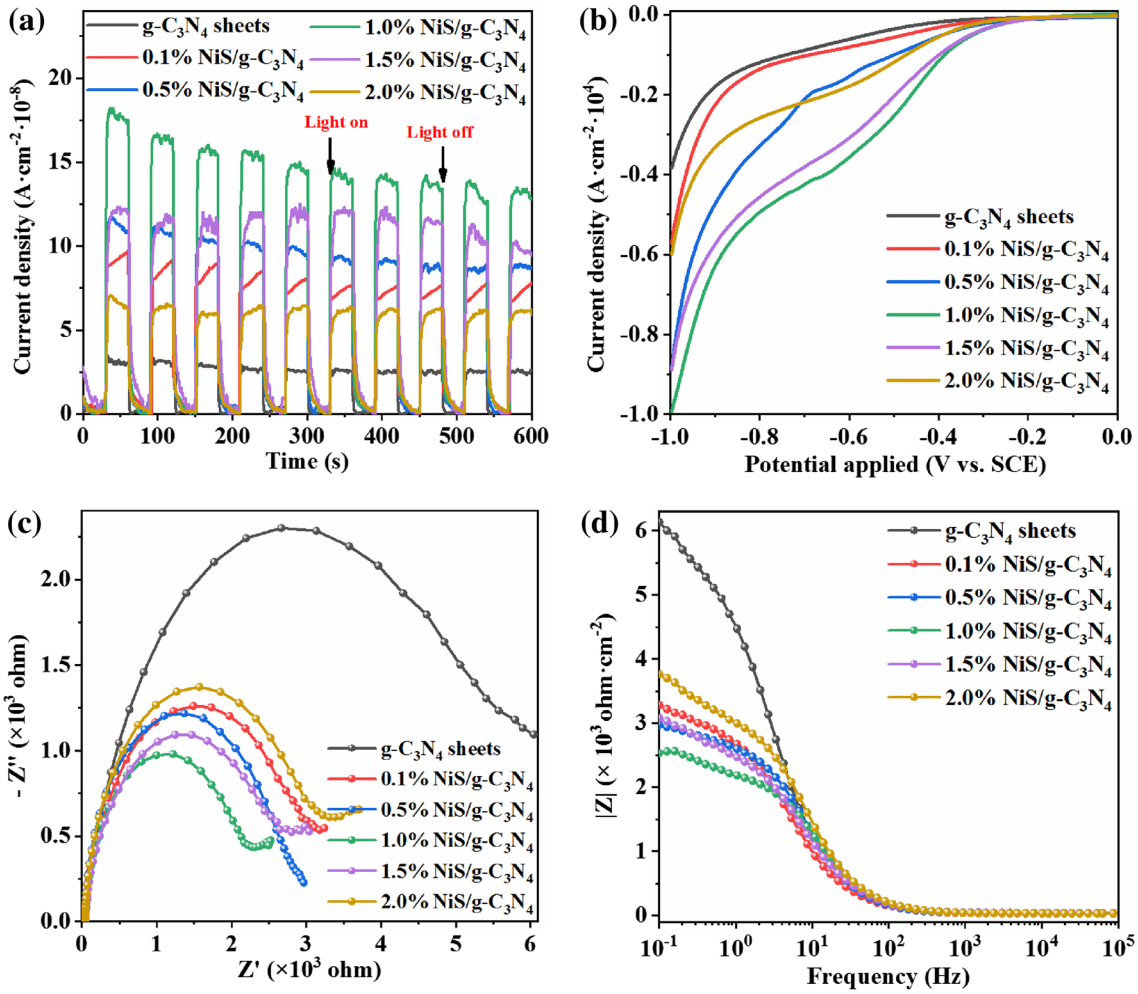

Fig. 5 **a** Transient I–t curves; **b** LSV polarization; **c** EIS Nyquist plots and **d** Bode plots for g-C_3N_4 sheets and NiS/g-C_3N_4 hybrids

production is evidently enhanced after modified with NiS cocatalyst, suggesting the separation and migration efficiencies of photo-generated carries are improved significantly. The average hydrogen evolution rate on different samples are calculated, the results are illustrated in Fig. 6b. It is obviously that the hydrogen evolution rate of NiS/g-C_3N_4 hybrids increase from 855.3 to 1346.1 μmol h^{-1} g^{-1} with the increasing NiS loading weight from 0.5 to 1.0%. However, with further increase the loading weight of NiS cocatalyst, the photocatalytic hydrogen production of NiS/g-C_3N_4 hybrids is decreased. This decrement probably due to the masking effect arising from the excessive NiS covered on the surface of g-C_3N_4 sheets, which could shield the incident light, thus resulting in the lower efficiency of the photocatalytic hydrogen production. In a word, compared with the pristine g-C_3N_4 nanosheets, the enhancements of the hydrogen evolution performances for NiS/g-C_3N_4 hybrids indicate that NiS is an efficient cocatalyst which can drastically improve the photocatalytic hydrogen evolution performance in the practical application.

In order to further evaluate the visible light utilization of catalysts, the AQE values of the hydrogen evolution on g-C_3N_4 sheets and NiS/g-C_3N_4 hybrids were calculated. One can see in Fig. 6c that the change trend of the AQE is consistent with the hydrogen evolution rate. The pure g-C_3N_4 sheets exhibit a negligible AQE value, further suggesting that the pristine g-C_3N_4 sheets have almost no hydrogen evolution capability under the visible light. The AQE value of 0.1% NiS/g-C_3N_4 hybrids is 4.67%, and continually increase to 7.67% when the loading weight of NiS cocatalyst up to 1.0 wt%, which is the highest value over all samples. Apart from the hydrogen production ability, the stability is also an important factor in the practical application. The reusability of the optimized sample (1.0% NiS/g-C_3N_4) was evaluated under the same reaction condition. According to the results (Fig. 6d), one can see that the hydrogen evolution of the catalyst does not show significant reduction after five cycles,

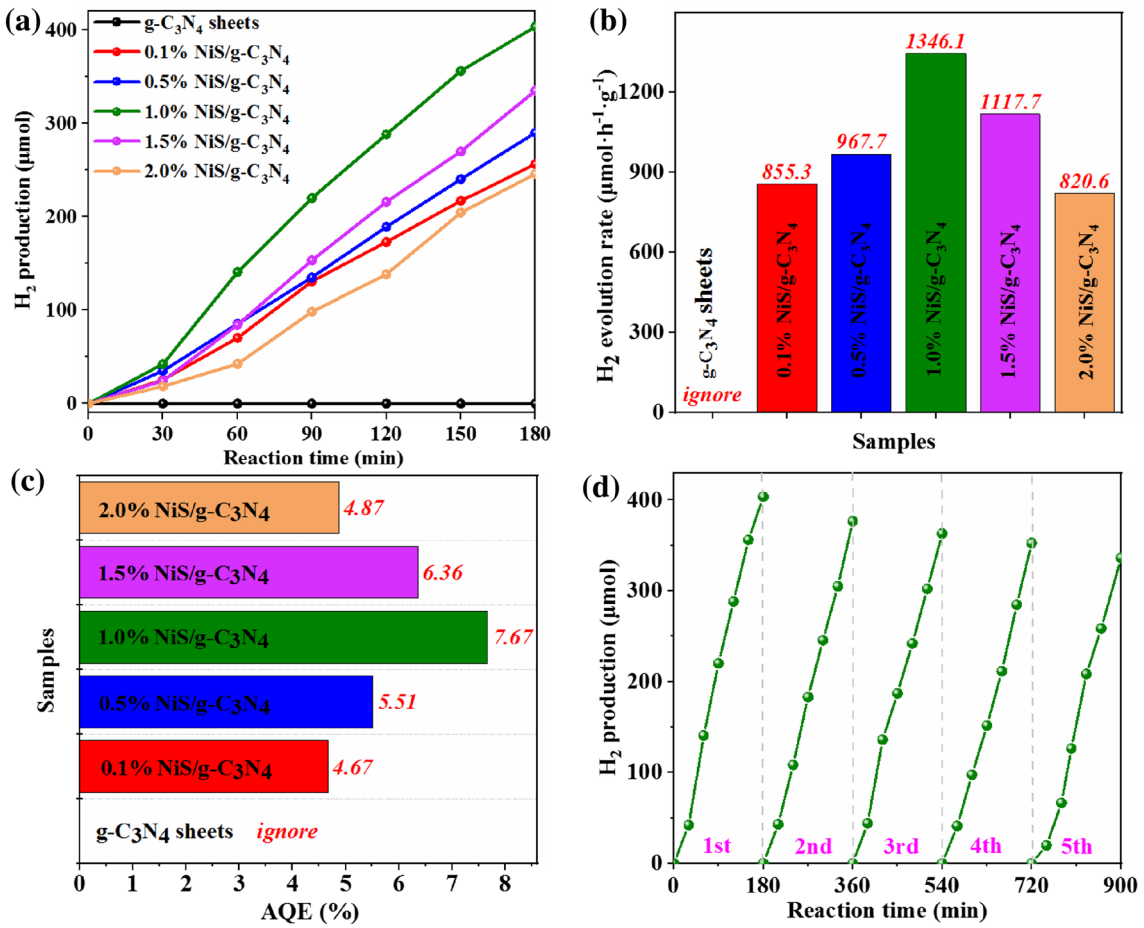

Fig. 6 **a** Time-dependent amount, **b** hydrogen production rates by the as-prepared samples, **c** calculated hydrogen evolution AQE of the catalysts and **d** cyclic hydrogen evolution curves for 1.0% NiS/g-C_3N_4 hybrids under visible light irradiation ($\lambda \geq 400$ nm) in presence of 15 vol% TEOA solution

suggesting that the robust heterogeneous junction catalysts have been established during the preparation process.

In order to investigate key factors playing critical roles in catalysts, the quantitative relationships between the properties of the catalysts and the hydrogen evolution activity has been explored, and the results are shown in Figure S7. The results revealed that the key factors playing critical roles in catalysts are the separation and migration efficiency of the e^-/h^+ pairs. In addition, a comparison of our present results with other similar investigations in literatures is provided. The 1.0% NiS/g-C_3N_4 photocatalyst used in this study is compared to some other photocatalysts as shown in Table S2. Moreover, a comparison of the effects of different based-materials (bulk g-C_3N_4 *vs* g-C_3N_4 sheets) and synthesis method (photodeposition vs hydrothermal) on hydrogen evolution properties have also been provided, as shown in Figure S8. Overall, the photocatalysts in our work show relatively higher hydrogen production activity.

3.6 Proposed Mechanisms for Formation and Hydrogen Evolution

According to the literatures [37, 44, 45] and the photochronopotentiometry characterization results (Figure S9), a possible formation mechanism of the catalyst during the photochemical deposition process was proposed (Scheme S1). Scheme S2 shows the standard electrode potential of the related substances. The reduction potential of Ni^{2+} to Ni^0 is about − 0.26 V, while the CB of g-C_3N_4 situates at − 1.30 eV. As a result, the photo-generated electrons have enough overpotential to reduce Ni^{2+} to Ni^0 to yield NiS particles on the outlet point of g-C_3N_4 sheets. But compared to the reduction potential of H^+ to H_2, it does not have enough

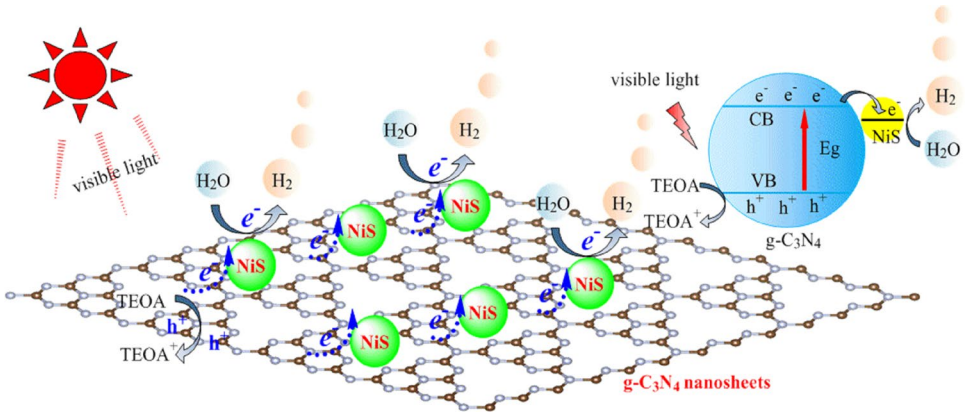

Fig. 7 Proposed separation and transfer mechanism of photo-generated charges over NiS/g-C_3N_4 hybrids for hydrogen evolution

competitiveness, so ethanol is used as a solvent in the preparation process to reduce the concentration of H^+. The ethanol also acts as the sacrificial reagent to consuming the photo-generated holes during the photodeposition process. g-C_3N_4 has a special 2D structure with few exposed chemical bonds on the surface, making it difficult to recombine with other substances. However, by employing the "in situ" photochemical deposition method, the NiS particles could be tightly loading on the surface of g-C_3N_4 sheets. The Ni^{2+} first was reduced to Ni_{ad} under the light irradiation by photo-generated electrons; NiS immediately formed at the Ni_{ad} site due to the presence of the dissolved Sulfur. Through this way the NiS was selectively deposited at the position where the electrons generated, an internal electric field was built between the interface of NiS and g-C_3N_4, thus the robust heterojunction was formed.

Based on the above discussions, the separation and migration mechanism of photo-generated charges over NiS/g-C_3N_4 hybrids was proposed, as shown in Fig. 7. As a semiconductor, the g-C_3N_4 sheets could be excited by visible light to generate the e^-/h^+ pairs. Theoretically speaking, the pure g-C_3N_4 sheets have sufficient capacity for water splitting arise from the suitable edge of CB and VB. However, the g-C_3N_4 sheets almost show the negligible yield of hydrogen production in the practical application, which mainly on account of the fast recombination of photo-generated carriers inside the catalyst. According to the literatures [46–48], there is a preferred charge accumulation in the g-C_3N_4 catalyst. Therefore, during the photochemical deposition process, the NiS nanoparticles are precisely deposited at the active sites where the photo-generated electrons ready to transfer to the g-C_3N_4 surface. Thus, by directing the flow of electrons, the separation of e^-/h^+ pairs are realized. The specific direction of charges transfer is shown in Figure S10. After trapping electrons, NiS forms the intermediate HNiS by absorption-reduction of a H^+ at first, and then electrochemically releases hydrogen with the reduction of another H^+ [34]. On the other hand, to further prevent the recombination of e^-/h^+ pairs, TEOA are used during the hydrogen evolution process, which act as the sacrifice reagent to consume the photo-generated holes. In a word, the photocatalytic hydrogen evolution performances of the catalysts depend on the generation and separation efficiency of photoelectrons, which ultimately result from the robust and precise heterojunction between NiS cocatalyst and g-C_3N_4 sheets.

4 Conclusions

In summary, the g-C_3N_4 nanosheets were successfully prepared by a thermal oxidation etching approach from bulk g-C_3N_4. Moreover, by using a facile photochemical deposition method, the Ni^{2+} is reduced into Ni^0 to from NiS and selectively deposited at the electron transfer site of g-C_3N_4 sheets. The NiS/g-C_3N_4 hybrids show highly efficient on hydrogen evolution in a TEOA aqueous solution under the visible light irradiation. The hydrogen production rate reached an optimum value when the loading amount of NiS is 1.0 wt%, which could achieve to be 1346.1 μmol h^{-1} g^{-1} with an AQE of 7.67%. According to the results of the above measurements, the enhanced hydrogen generation of the NiS/g-C_3N_4 hybrids was attributed to the NiS cocatalyst tightly loading on the surface of g-C_3N_4 sheets, which act as the electron trapping center and the targeting active sites for hydrogen evolution. This report providing a new insight realized the precise deposition, anchoring the NiS cocatalysts on to the outlet points of photo-generated electrons, thus enhancing the photocatalytic hydrogen evolution performance. This attempt could also be applied to loading other cocatalysts onto 2D materials.

Acknowledgements This work was financially supported by the National Key R&D Program of China (No. 2019YFA0210003) and the National Natural Science Foundation of China (No. 11927808).

References

1. Hosseini SE, Wahid MA (2016) Renew Sustain Energy Rev 57:850–866
2. Voiry D, Shin HS, Loh KP, Chhowalla M (2018) Nat Rev Chem 2:0105
3. Jing L, Zhu R, Phillips DL, Yu JC (2017) Adv Funct Mater 27:1703484
4. Sun Z, Zhu M, Fujitsuka M, Wang A, Shi C, Majima T (2017) ACS Appl Mater Interfaces 9:30583–30590
5. Wu Y, Wang Y, Di A, Yang X, Chen G (2018) Catal Lett 148:2179–2189
6. Wei RB, Huang ZL, Gu GH, Wang Z, Zeng L, Chen Y, Liu ZQ (2018) Appl Catal B 231:101–107
7. Han B, Liu S, Zhang N, Xu YJ, Tang ZR (2017) Appl Catal B 202:298–304
8. Zhao CW, Li YA, Wang XR, Chen GJ, Liu QK, Ma JP, Dong YB (2015) Chem Commun 51:15906–15909
9. Liang Y, Shang R, Lu J, An W, Hu J, Liu L, Cui W (2019) Int J Hydrogen Energy 44:2797–2810
10. Zhu Z, Kao CT, Tang BH, Chang WC, Wu RJ (2016) Ceram Int 42:6749–6754
11. Ma J, Tan X, Yu T, Li X (2016) Int J Hydrogen Energy 41:3877–3887
12. Zhang J, Sun J, Maeda K, Domen K, Liu P, Antonietti M, Fu X, Wang X (2011) Energy Environ Sci 4:675–678
13. Fang J, Fan H, Li M, Long C (2015) J Mater Chem A 3:13819–13826
14. Guo F, Shi W, Zhu C, Li H, Kang Z (2018) Appl Catal B 226:412–420
15. Zhao S, Zhang Y, Zhou Y, Wang Y, Qiu K, Zhang C, Fang J, Sheng X (2018) Carbon 126:247–256
16. Zhao Y, Wei R, Feng X, Sun L, Liu P, Su Y, Shi L (2016) ACS Appl Mater Interfaces 8:21555–21562
17. Wang XJ, Tian X, Sun YJ, Zhu JY, Li FT, Mu HY, Zhao J (2018) Nanoscale 10:12315–12321
18. Wang H, Wang B, Bian Y, Dai L (2017) ACS Appl Mater Interfaces 9:21730–21737
19. Chen XF, Zhang JS, Fu XZ, Antonietti M, Wang XC (2009) J Am Chem Soc 131:11658–11659
20. Niu P, Zhang L, Liu G, Cheng H-M (2012) Adv Funct Mater 22:4763–4770
21. Schwinghammer K, Mesch MB, Duppel V, Ziegler C, Senker J, Lotsch BV (2014) J Am Chem Soc 136:1730–1733
22. Xu Z, Zhuang C, Zou Z, Wang J, Xu X, Peng T (2017) Nano Res 10:2193–2209
23. Lu X, Xu K, Chen P, Jia K, Liu S, Wu C (2014) J Mater Chem A 2:18924–18928
24. Zhang X, Xie X, Wang H, Zhang J, Pan B, Xie Y (2013) J Am Chem Soc 135:18–21
25. Ma L, Fan H, Wang J, Zhao Y, Tian H, Dong G (2016) Appl Catal B 190:93–102
26. Liang S, Xia Y, Zhu S, Zheng S, He Y, Bi J, Liu M, Wu L (2015) Appl Surf Sci 358:304–312
27. Fu Y, Huang T, Jia B, Zhu J, Wang X (2017) Appl Catal B 202:430–437
28. Ge L, Han C, Liu J, Li Y (2011) Appl Catal A 409:215–222
29. Li Z, Wu L, Wang L, Gu A, Zhou Q (2017) Electrochim Acta 231:617–625
30. Li C, Du Y, Wang D, Yin S, Tu W, Chen Z, Kraft M, Chen G, Xu R (2017) Adv Funct Mater 27:1604328
31. Li C, Wang H, Naghadeh SB, Zhang JZ, Fang P (2018) Appl Catal B 227:229–239
32. Xin Y, Lu Y, Han C, Ge L, Qiu P, Li Y, Fang S (2017) Mater Res Bull 87:123–129
33. Hong J, Wang Y, Wang Y, Zhang W, Xu R (2013) Chemsuschem 6:2263–2268
34. Chen Z, Sun P, Fan B, Zhang Z, Fang X (2014) J Phys Chem C 118:7801–7807
35. He K, Xie J, Li M, Li X (2018) Appl Surf Sci 430:208–217
36. Ge L, Han C, Xiao X, Guo L (2013) Appl Catal B 142:414–422
37. Fujii M, Nagasuna K, Fujishima M, Akita T, Tada H (2009) J Phys Chem C 113:16711–16716
38. Dong F, Li Y, Wang Z, Ho W-K (2015) Appl Surf Sci 358:393–403
39. Wen J, Xie J, Zhang H, Zhang A, Liu Y, Chen X, Li X (2017) ACS Mater Interfaces 9:14031–14042
40. Mao ZY, Chen JJ, Yang YF, Wang DJ, Bie LJ, Fahlman BD (2017) ACS Appl Mater Interfaces 9:12427–12435
41. Wen J, Xie J, Yang Z, Shen R, Li H, Luo X, Chen X, Li X (2017) ACS Sustain Chem Eng 5:2224–2236
42. Sing KSW, Everett DH, Haul RAW, Moscou L, Pierotti RA, Rouquerol J, Siemieniewska T (1985) Pure Appl Chem 57:603–619
43. Basu M, Zhang ZW, Chen CJ, Lu TH, Hu SF, Liu RS (2016) ACS Appl Mater Interfaces 8:26690–26696
44. Jiang W, Zong X, An L, Hua S, Miao X, Luan S, Wen Y, Tao FF, Sun Z (2018) ACS Catal 8:2209–2217
45. Jin-nouchi Y, Akita T, Tada H (2010) ChemPhysChem 11:2349–2352
46. Ma X, Lv Y, Xu J, Liu Y, Zhang R, Zhu Y (2012) J Phys Chem C 116:23485–23493
47. Guan L, Chen X (2018) ACS Appl Energy Mater 1:4313–4320
48. Li Q, Jiang J, Lin B, Ding D, Xu H, Wang P, Chen Y (2019) Catal Lett 149:3296–3303

Affiliations

Xiao Lin[1] · Shiwen Du[1] · Chunhe Li[1] · Guojun Li[1] · Youji Li[2] · Feitai Chen[2] · Pengfei Fang[1]

✉ Pengfei Fang
fangpf@whu.edu.cn

[1] School of Physics and Technology, Key Laboratory of Nuclear Solid State Physics Hubei Province, Wuhan University, Wuhan 430072, China

[2] College of Chemistry and Chemical Engineering, Jishou University, Jishou 416000, China